

# Graphene Nanostructuring for Energy Conversion at Nanoscale

Ivan Giambrone

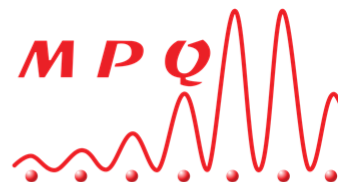
Supervisors:

Maria Luisa Della Rocca

Carlo Ricciardi

M2 - Quantum Devices

International Program NanoQuad



Politecnico  
di Torino

Paris  
June 2022

## Contents

<b>1</b>	<b>Introduction</b>	<b>3</b>
<b>2</b>	<b>Presentation of the lab</b>	<b>4</b>
<b>3</b>	<b>State of the art</b>	<b>5</b>
3.1	Graphene as thermoelectric material . . . . .	5
3.2	Seebeck effect in graphene . . . . .	7
3.3	Thermal conductivity of graphene . . . . .	8
<b>4</b>	<b>Device fabrication and characterization</b>	<b>9</b>
4.1	Clean-room nanofabrication . . . . .	9
4.2	AFM analysis . . . . .	12
<b>5</b>	<b>Thermoelectric characterization protocol</b>	<b>13</b>
5.1	Thermometers calibration . . . . .	14
5.2	Temperature gradient calibration . . . . .	14
5.3	Electrical and thermoelectric measurements . . . . .	15
5.4	Seebeck coefficient measurement . . . . .	16
5.5	Thermoreflectance Measurements . . . . .	17
<b>6</b>	<b>Results and discussion</b>	<b>20</b>
6.1	Electric and thermoelectric properties . . . . .	20
6.2	Power Factor . . . . .	22
6.3	Thermoreflectance results . . . . .	22
<b>7</b>	<b>Conclusions and future perspectives</b>	<b>24</b>

## 1 Introduction

Electronic devices at the basis of all the most important technological and industrial processes require a high amount of energy to work, which is supposed to increase in the next years<sup>[1],[2]</sup>. However, great part of the injected power is dissipated in form of heat, becoming difficult to be recovered<sup>[3]</sup>. To pursue this aim, one possibility is to exploit the mechanism of thermoelectric energy conversion, which is the process of conversion of thermal energy into electrical energy. This is possible by means of the Thermoelectric Effect (TE)<sup>[4]</sup>, i.e. the ability of certain materials of creating a potential difference when a temperature gradient is present, and conversely, the creation of a temperature gradient generated by a current flow, phenomenon known as Peltier Effect. The physical mechanism explaining the thermoelectric power generation is essentially the diffusion<sup>[5]</sup> of charge carriers from the hottest to the coldest side of the material.

The temperature to voltage conversion is quantified by the Seebeck coefficient<sup>[6]</sup>, also known as Thermoelectric Power,

$$S = -\frac{\Delta V}{\Delta T}$$

where  $\Delta V$  and  $\Delta T$  are the potential difference and the temperature gradient across the material, respectively<sup>[7]</sup>. The Seebeck coefficient can be simply viewed as the entropy carried per unit charge in the material<sup>[8]</sup>.

The experimental efficiency of a TE power generator is defined as  $\eta = P/Q$ , with P the electrical power output and Q the rate of heat injected in the system<sup>[9]</sup>. Due to irreversible losses such as Joule heating, its value cannot realistically reach the theoretical Carnot efficiency<sup>[10]</sup>  $\eta = 1 - T_c/T_h$ , with  $T_c$  and  $T_h$  the temperatures at the cold and hot ends of the device. The maximum obtainable experimental efficiency<sup>[11]</sup> can be written as

$$\eta_{max} = \left(1 - \frac{T_c}{T_h}\right) \frac{\sqrt{1 + ZT} - 1}{\sqrt{1 + ZT} + \frac{T_c}{T_h}}$$

where  $ZT$  is the so-called thermoelectric figure of merit, defined at a given temperature  $T$  as

$$ZT = \frac{S^2 \sigma T}{\kappa}. \quad (1)$$

with  $\sigma$  and  $\kappa$  are the electrical and total thermal conductivities (including the electronic  $\kappa_e$  and phononic  $\kappa_{ph}$  components) of the material, respectively. In practical devices maximum  $ZT$  are of the order of  $\simeq 1$ , which corresponds to a low efficiency  $\eta \simeq 0.04$  if considering example values of  $T_{cold}=25^\circ\text{C}$  and  $T_{hot}=100^\circ\text{C}$ . The figure of merit is the essential parameter to maximize in order to obtain the best performance in thermoelectric energy conversion<sup>[12]</sup>. The term  $S^2 \sigma$  is called power factor (PF) and it is also often used as a metric parameter; its maximization has great relevance for obtaining the highest possible figure of merit.

Naturally, optimal thermoelectric materials are supposed to have high electrical conductivity, in order to allow easy carrier motion, and low thermal conductivity, to sustain a temperature gradient across them, as well as high Seebeck coefficient. Unfortunately, it is well-known that the electrical conductivity  $\sigma$  and the electronic component of the thermal conductivity  $\kappa_e$  are related

by the Wiedemann-Franz law,  $\sigma/\kappa_e = LT$  (where  $L$  is the Lorentz number  $2.44 \times 10^{-8} V^2 K^{-2}$ )<sup>[13]</sup>, which represents a limit in the optimization of  $ZT$ . Furthermore, the physical quantities defining  $ZT$  present an interconnected behaviour as a function of the carrier concentration, as shown in Fig.1. The maximization of the power factor is a relevant problem since the Seebeck coefficient and the electrical conductivity depend on it in a reciprocal way<sup>[14],[15]</sup>.

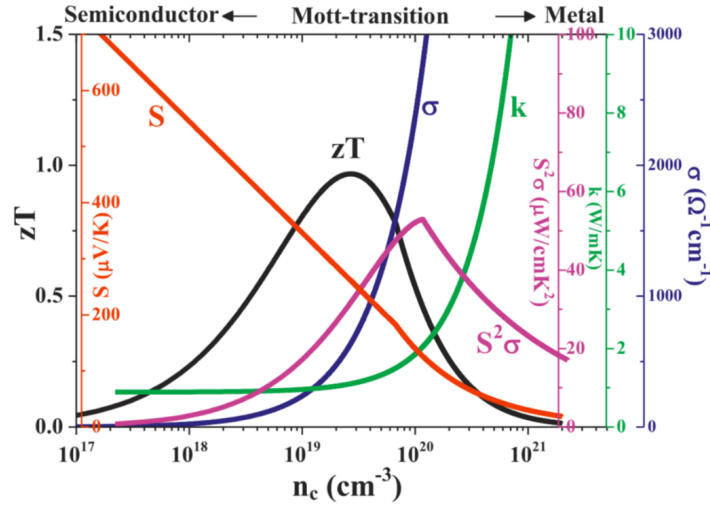


**Figure 1:** Seebeck coefficient, electrical and thermal conductivity as a function of the carrier concentration, and the resulting power factor and figure of merit. Extracted from [15].

Then, there is an optimal carrier density to maximize the thermoelectric properties, which is strictly determined by the material properties<sup>[2]</sup>. Since the beginning of '2000, it has been shown that reduced dimensions can be beneficial for energy conversion efficiency<sup>[16],[17],[18]</sup>. As a consequence, modifications in the material band structure<sup>[12]</sup> and the geometry<sup>[19]</sup> of the final device could allow greater PF and, as a consequence, improved thermoelectric power generation capability.

The focus of my work during this internship has been exploring new routes of engineering low dimensional (2D) materials to improve their thermoelectric properties.

## 2 Presentation of the lab

The Internship project has been led at the MPQ (Matériaux et Phénomènes Quantiques) lab, specialized in the study of innovative quantum materials and devices. In particular, I worked in the TELEM team (Transport Electronique à L'Echelle Moléculaire), where the research is focused on the study of charge, heat and spin transport in 2D materials and Van der Waals hetero-structures. The team has at disposal a cleanroom for the fabrication of the desired devices, and many facilities in the lab, such as high and low temperature experimental set-ups for the electric and thermal characterizations.

### 3 State of the art

#### 3.1 Graphene as thermoelectric material

In order to maximize the figure of merit, one of the most efficient ways is to increase the PF by raising the Seebeck coefficient. Potentially, this can be achieved in low dimensional systems, such as 2D materials. The reason for this can be intuitively found in the expression of the Seebeck coefficient given by the Mott formula<sup>[20]</sup>:

$$S = \frac{\pi^2}{3} \frac{k_B}{e} k_B T \frac{1}{\sigma(E)} \frac{d\sigma(E)}{dE}. \quad (2)$$

where  $k_B$  is the Boltzmann constant,  $e$  the electron charge,  $T$  the temperature and  $\sigma(E)$  the energy dependent electrical conductivity.  $\sigma(E)$  is equal to  $\sigma(E) = en(E)\mu(E)$ , with  $\mu(E)$  the mobility and  $n(E)$  the density of charge carriers. Since  $n(E) = g(E)f(E)$ , where  $g(E)$  is the density of states and  $f(E)$  is the Fermi distribution function, any variation of the density of states such as the appearance of sharp features due to a reduced system dimensionality is supposed to enhance the Seebeck coefficient<sup>[20]</sup>.

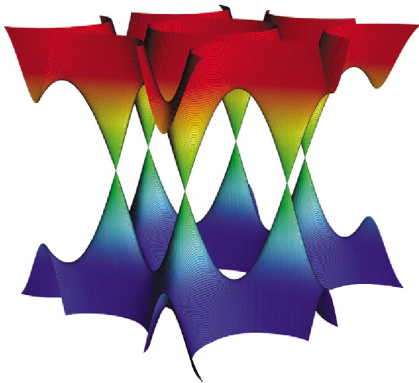


**Figure 2:** Graphene band structure. Extracted from [21].

The 2D material of choice during my work has been graphene, whose structure is made of one layer of carbon atoms disposed in a honeycomb lattice. Its incredible properties allowed it to be one of the most studied materials in the past years since its first isolation in 2004<sup>[22]</sup>. Graphene possesses a band structure as the one shown in Fig.2, where the conduction and valence band touch in correspondence of the so-called Dirac points<sup>[21]</sup>. This leads to very unprecedented electronic properties: graphene is a semimetal or a zero gap material, well described by theories for massless relativistic particles<sup>[23]</sup>.

Graphene is not in principle the best 2D material to chose for thermoelectric energy conversion, since even if it can reach a high electrical conductivity<sup>[24]</sup>, and quite high Seebeck coefficient<sup>[8]</sup>, it possesses an extraordinary high phonon contribution to the thermal conductivity. In fact, while the graphene cross-plane thermal conductivity  $\kappa_{\perp}$  is strongly limited by the weak interplane Van der Waals bonds, the in-plane component  $\kappa_{//}$  is one of the highest of any known material, reaching values as high as 2000-4000  $\text{Wm}^{-1}\text{K}^{-1}$  in the suspended case<sup>[25]</sup>. This is due to the very strong bonding of light atoms, allowing large phonon mean free path which can reach several hundreds of nm<sup>[26]</sup>. Anyway graphene, as any other 2D material, is extremely sensitive to the environment: the presence of a substrate and a surrounding atmosphere can induce charge doping, as well as electrical contacts and interfaces produce orbital hybridization effects modifying its electronics properties<sup>[27]</sup>. Furthermore it has been demonstrated that when supported or in presence of defects, graphene thermal conductivity can be reduced by a factor higher than 10<sup>[28],[29]</sup> and in general any additional disorder or even residue from nanofabri-

cation process will introduce more scattering for phonons and electrons<sup>[20]</sup>. This means that apart from their physical properties in the isolated form, 2D material in general can profoundly be modified when engineered in real devices. Therefore, device engineering represents an useful approach to optimize thermoelectric energy conversion at nanoscale. One possible way to implement device engineering is by changing the geometrical properties of the used material in order to achieve the direct modification of its electronic and phononic density of states<sup>[5]</sup> as well as to directly control the electron and phonon diffusion<sup>[25]</sup>. Following this aim, during my internship, graphene, in the form of multilayer, has been nanomeshed with a triangular lattice of pores as illustrated in Fig.3, where  $h$  is the minimum distance between two pores edges, called neck width;  $L$  is the distance between two pores centers and  $R$  is the pore radius. Such nanomeshed graphene is inserted in solid state devices for electric and thermoelectric characterization.

Graphene nanomeshes (GNMs) are thus defect-engineered graphene nanostructures consisting of a periodic arrangement of nano-scale holes or pores in the graphene lattice<sup>[31]</sup>. If the neck widths are less than 10 nm, the GNM mimicks a dense arrays of ordered nanoribbons, allowing a sizable bandgap opening. This newly formed band gap could allow the separation of electron and hole contribution to the Seebeck signal<sup>[20]</sup>.

The possibility of controlling pore size and arrangement gives to GNMs a great potential for thermoelectric energy conversion. Beside inducing a bandgap<sup>[32]</sup>, nanomeshing can induce localization effects due to edge disorder<sup>[31]</sup>. Heat diffusion is linked to the propagation of phonon waves, which are back scattered by the pore-edges: the incoming wave and the one reflected by the defect may cancel out leading to an interference mechanism that could modify the phonon dispersion relation introducing a phononic band gap<sup>[5]</sup>. Furthermore, gas molecules adsorbed by the pore-edges during the nanostructuring process, for example by using oxygen plasma, could induce pore-edge charges that could enhance carrier scattering<sup>[5]</sup> and induce an increased Seebeck effect by filtering out the low-energy carriers<sup>[33],[34]</sup>. Nanomeshing represents a way to increase phonon scattering and so reducing the thermal conductivity<sup>[26]</sup>. In graphene phonon diffusion occurs over distances typically one order of magnitude higher than electronic diffusion<sup>[35],[25]</sup>. In general, introducing sub-10 nm patterns, the quantum confinement can simultaneously control the electronic and phononic band structures, whereas sub-100 nm patterns only reduce the mean free path of the phonon and scarcely affect the electric and thermoelectric properties<sup>[25]</sup>.

My internship work has represented the first attempt in the team of graphene nanostructuring. I have fabricated and characterized multilayer graphene nanomeshed structures with typical pore-edge distances of the order of  $\sim 150$  nm. This is not yet the optimal dimension to strongly modify the material properties, but still it has produced first interesting results.

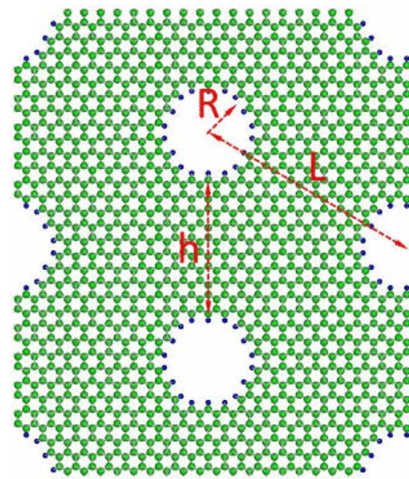


**Figure 3:** Graphene nanomesh, taken from [30].

### 3.2 Seebeck effect in graphene

The first remarkable measurement of TE properties of single layer graphene has been published by Zuev et al. in 2009<sup>[8]</sup>. The device (Fig.4a) consisted of a graphene flake on top of a Si/SiO<sub>2</sub> substrate acting as a backgate, with a metallic nanowire in proximity of the flake having the function of local heater. On top of the graphene, two thermometers are also deposited realizing the so-called mesoscopic device configuration for thermoelectric measurements.

The measured Seebeck coefficient as a function of the gate voltage at different temperatures is shown in Fig.4b. Close to the Charge Neutrality Point (CNP), as the gate voltage tends to zero, both electrons and holes give a contribution (opposite in sign) to the Seebeck, so that it tends to zero. Far from the CNP, the system is degenerated and S is greater, and, as expected from equation 2, increases with temperature.

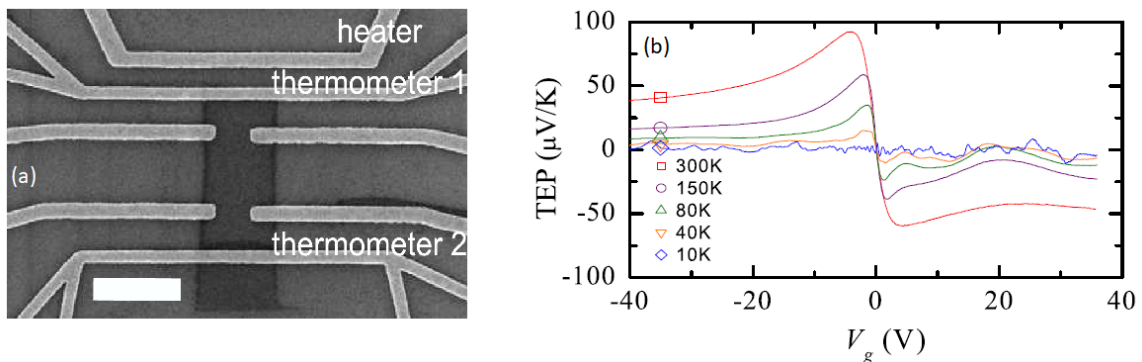


**Figure 4:** (a) GN based devices for thermoelectric measurements. (b) Thermoelectric Power (Seebeck Coefficient) measured on the device in (a) as a function of the applied gate voltage. Extracted from [8].

In the more recent work of Duan et al.<sup>[36]</sup>, a similar configuration has been used, but with an insulating 2D layer of hBN (hexagonal boron nitride) which decouples the graphene flake from the Si/SiO<sub>2</sub> substrate (device in Fig.5a). The main measured system consists of a Van der Waals heterostructure, that is a stack of 2D materials whose properties can be engineered by the selected sequence of layers.

hBN has a honeycomb lattice similar to the one of graphene, but with alternating B and N atoms: this provides the breaking of the sublattice symmetry necessary to open a gap, which reaches a value of  $\sim 5.97eV$ <sup>[37]</sup>. Furthermore, high thermal stability (up to 1000 °C in air) and excellent mechanical strength (elastic constant of 220–510 N/m and Young’s modulus  $\sim 1.0$  TPa) allow it to be a great choice as insulating 2D layer<sup>[37]</sup>.

The SiO<sub>2</sub> substrate limits graphene mobility due to the high scattering rate induced by surface charge states and impurities for Coulomb scattering. A hBN substrate instead, being quite inert and free of surface charge states, would not produce much potential fluctuation and as a consequence the mobility of the upstanding graphene tends to decrease less. In the presence of hBN the Seebeck signal is boosted, as shown in Fig.5b. This work has clearly demonstrated that a decoupling layer of hBN can improve electric and thermoelectric properties of graphene, and so, this configuration is particularly appropriate in supported (on substrate) graphene based devices, which has been the

configuration of choice during my work.

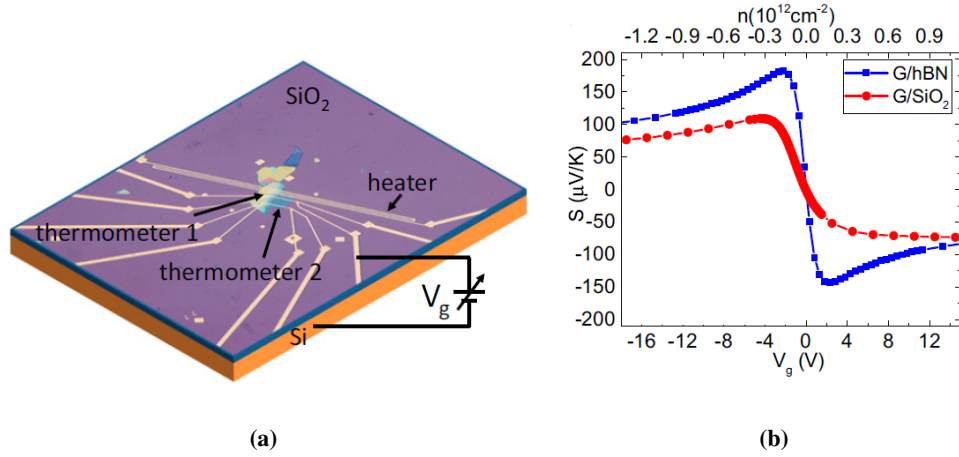


**Figure 5:** (a) hBN/GN based device for thermoelectric measurements. (b) Measured  $S$  for devices with and without hBN layer as a function of the applied gate voltage. Extracted from [36].

### 3.3 Thermal conductivity of graphene

Many experiments have been carried on in the last years to quantify the thermal conductivity of graphene and carbon based materials in general, for which a summary of the trends is shown in Fig.6. Values of  $\kappa$  for suspended single layer graphene (SLG) for a range of temperatures between 300 K and 600 K has been extracted<sup>[38],[39]</sup> by means of the Raman Optothermal Thermometry technique. The obtained conductivities fall in the range of 2000-4000  $\text{Wm}^{-1}\text{K}^{-1}$  for room temperature, and then decreasing to 700-1500  $\text{Wm}^{-1}\text{K}^{-1}$  around 500 K.

These values should be close to the purely theoretical ones<sup>[26]</sup>, for which the thermal conductivity is only limited by crystal anharmonicity<sup>[40]</sup> and electron-phonon scattering<sup>[26]</sup>. However, in practice, devices always exploit graphene in different conditions for which the heat transport is strongly modified by the environment and material defects. Seol et al.<sup>[41],[42]</sup> have measured the thermal conductivity of a supported graphene flake on top of a  $\text{SiO}_2$  substrate. A lowering of almost one order of magnitude is found, with a value for  $\kappa \sim 600 \text{Wm}^{-1}\text{K}^{-1}$ .

Great modifications can be furthermore introduced in a few layer graphene (FLG). In a suspended FLG, in fact, Jang et al.<sup>[43]</sup> have found by a modified T-bridge micro-resistance thermometry technique  $\kappa \sim 300\text{-}400 \text{Wm}^{-1}\text{K}^{-1}$  for a 2-4

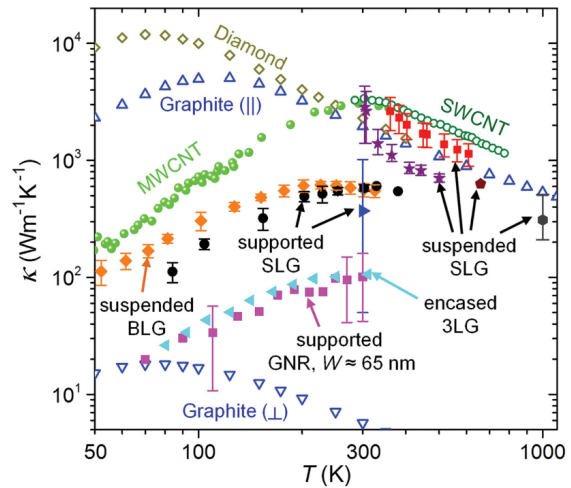


**Figure 6:** Thermal conductivity behavior as a function of the temperature for different carbon based materials. Extracted from [26].

layers flake, and the value increases to  $\sim 600 \text{ Wm}^{-1}\text{K}^{-1}$  when raising the number of layers to 8. This increment could represent a tendency to recover the high value of graphite thermal conductivity. This tendency is also present in the results reported by Sadeghi et al.<sup>[28]</sup>, for a supported multilayer graphene.

## 4 Device fabrication and characterization

In this paragraph, I will present the different steps of the device fabrication. The device consists of a thin metal gate on which a hBN/GN heterostructure is transferred. Two nanowires are deposited on the top, acting as local thermometers and electrodes. A third nanowire, electrically decoupled from the structure, allows for local heating.

### 4.1 Clean-room nanofabrication

The starting point for the device fabrication is a Si/SiO<sub>2</sub> substrate pre-patterned with Au contacts, as shown in Fig.7a, obtained by standard optical lithography and metal evaporation. The substrates are cleaned in successive baths of acetone and isopropanol, then dried by N<sub>2</sub> gas before nanofabrication.

In the central  $100 \times 100 \mu\text{m}^2$  area of the pre-patterned structure I fabricate the bottom metal gate and the local heater (separated by  $\sim 350 \text{ nm}$ ) by standard electron beam lithography (EBL) and metal deposition. A PMMA (Polymethyl Metacrilate)/Anisole solution (2:1) is spin coated (500 rpm for 5 s / 4000 rpm for 40 s) onto the device and, after a 180°C baking for 60 s, EBL is performed by means of a Zeiss scanning electron microscope (SEM). PMMA is removed in a 1:3 solution of MIBK (Methylisobutylketone)/isopropanol. A titanium/gold bilayer (Ti 5 nm / Au 35 nm) is deposited by an electron-beam evaporator (PLASSYS MEB550S) at a rate 0.04 nm/s, and a lift-off process of about 3 hours in acetone is needed to reveal the structure as shown in Fig.7b.

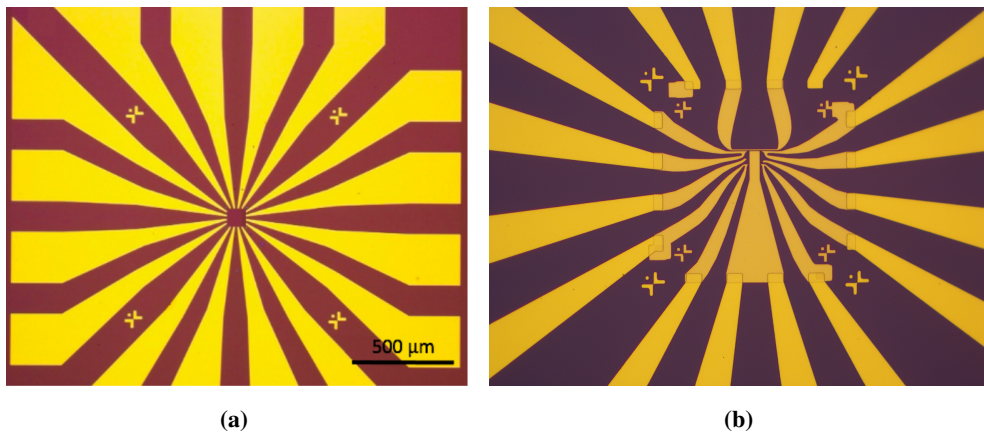


**Figure 7:** (a) Optical image of the Si/SiO<sub>2</sub> substrate pre-patterned with Au contacts. (b) Optical image of the deposited Ti/Au metallic gate.

The successive step consists in the dry-transfer of the 2D materials on the top of the metallic

gate and nano heater. I used hBN as a dielectric layer, allowing a capacitive coupling between the gate and the multilayer graphene, acting as active thermoelectric material. These 2D materials are first mechanically exfoliated over a Si/SiO<sub>2</sub> substrate, from which we pick-up the desired flake to be dropped-down over the sample. This process is achieved by using drops of PDMS (Polydimethylsiloxane) coated with PPC (Polypropylene carbonate). The drops are obtained by depositing on the ending part of a glass slide a solution (10:1) of SYLGARD 184 Base and SYLGARD 184 Curing Agent, previously dried at room temperature for ~6 hours. The slide is turned upside down so that the excess polymer falls out and is removed, leaving a cured drop on the glass slide, as shown in Fig.8a. The PPC is spin coated (500 rpm for 3 s / 2500 rpm for 40 s) on the drop.

To perform the pick-up of the 2D materials, the wafer with the exfoliated flakes is put on an heating plate, the center of the drop and the desired flake are aligned on the optical axis of a microscope by means of two micro-manipulators (Fig.8b). With a set temperature of 65°C, the drop is put in contact with the flake to catch it, by continuously adjusting the focal point. The drop-down of the flake over the gate is achieved by inverting the process. Once the flake is positioned over the gate, the temperature is raised to 95°C, so that the PPC on the drop melts and the flake is deposited. To remove the polymer left on the sample, a cleaning in acetone and isopropanol is performed. The result of the transfer process can be seen in Fig.9a, where the hBN and the GN flakes can be recognized by their light blue and dark blue color, respectively.

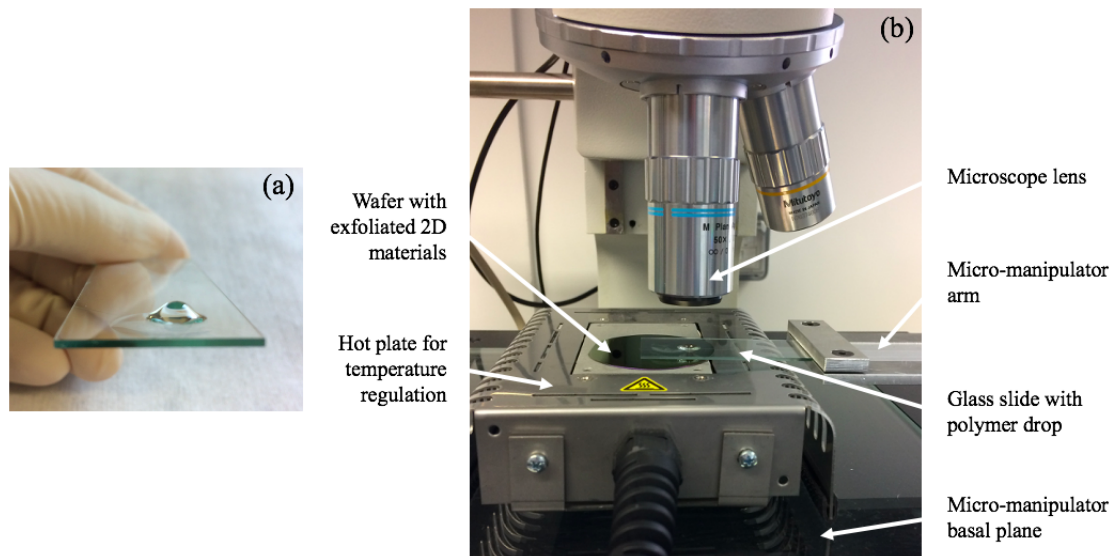


**Figure 8:** (a) PDMS/PPC drop on a glass slide. (b) Setup for the pick-up transfer, composed by a hot plate positioned onto an optical microscope micro-manipulator plate, and a micro-manipulator arm to regulate the position of the drop.

Successively, two Ti/Au (5 nm/75 nm) nanowires (5  $\mu$ m-long, 300 nm-wide) acting as metallic electrodes and local thermometers are deposited, with the same technique used for the metallic gate, as it can be seen in Fig.9b. Each nanowire has 4 contacts to precisely measure its resistance.

The fabrication of the nanomesh is the last step of the whole fabrication process and it was

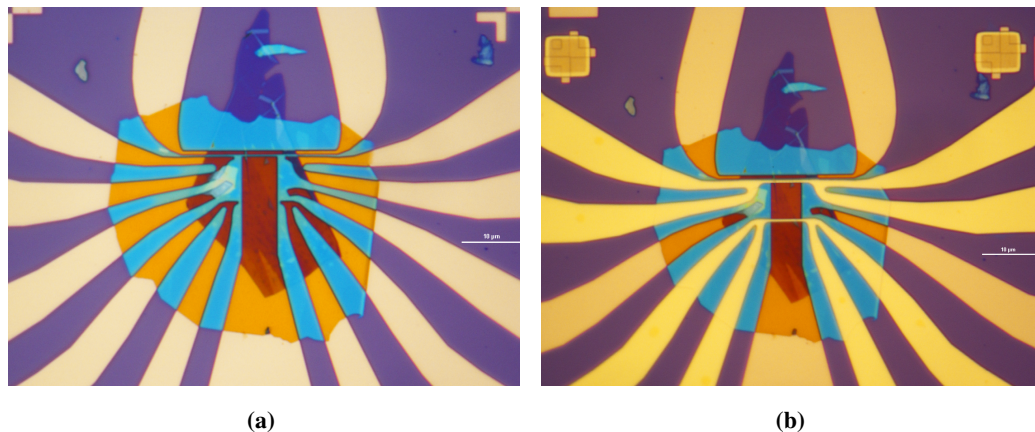


**Figure 9:** (a) Sample after the transferring of the hBN (light blue) and graphene (dark blue) flakes (b) Sample after thermometers deposition.

completely implemented with my arrival in the team. The optimization of the process has finally led to the solution proposed in ref.[44] and schematically illustrated in Fig.10. It is based on the use of a metallic aluminium thin layer mask to etch graphene. The sample is spin coated with a layer

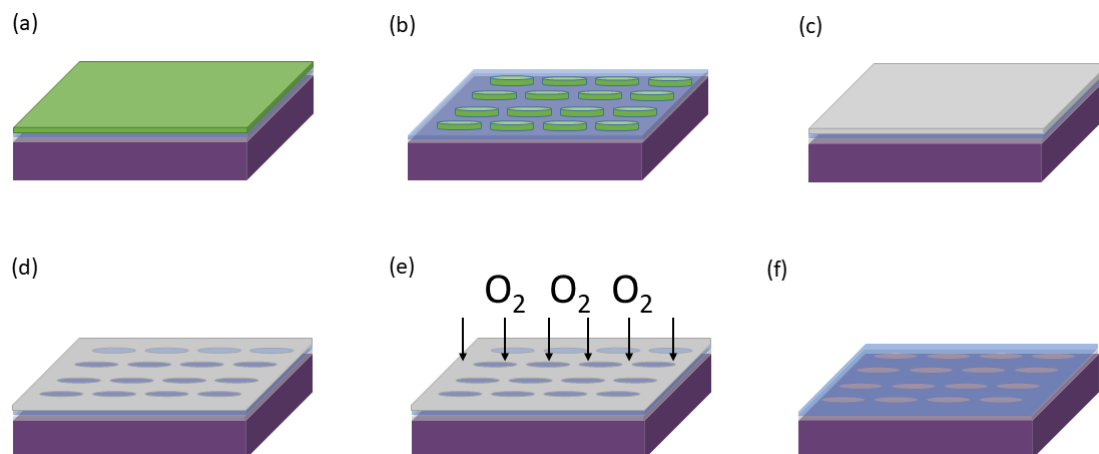


**Figure 10:** Schematic of the graphene nanomeshing procedure: (a) Ti Prime+CSAR62 is spin coated onto the sample and (b) then patterned in nanopillars. (c) A 7nm Al layer is deposited and (d) the lift off of the previously patterned resist is done, leaving an Al mask with holes. (e) Finally, oxygen plasma is used to etch the graphene into the holes and (f) the Al is then removed.

of Ti Prime (500 rpm/4000 rpm for 3s /30 s) acting as adhesion layer, and then with CSAR 62 (500 rpm/4000 rpm for 3 s /30 s) (Fig.10a). EBL is used to define a reversed nanomeshed mask. The exposed resist is developed in AR600-546 for 1 min, then in a solution of MIBK:isopropanol (1:3) for 30s and isopropanol for 30s. The revealed pattern is a network of nanopillars with diameter of  $\sim 390$  nm and pitch distance of  $\sim 160$  nm (Fig.10b). I successively deposit 7 nm of Al (Fig.10c) that, after lift off, reveal a thin metallic Al nanomeshed mask over the graphene layer (Fig.10d). In this case the lift-off is in butanone at 40°C, it lasts one day and requires 20sX4 final steps

in ultrasounds. A 40 seconds oxygen plasma treatment is done with a Corial 200R RIE etching system (Fig.10e) in order to etch the graphene not protected by the Al layer. Finally, the Al mask is removed (Fig.10f). The final result can be seen in Fig.11, showing an optical (Fig.11a) and SEM (Fig.11b) image of the nanomeshed device.

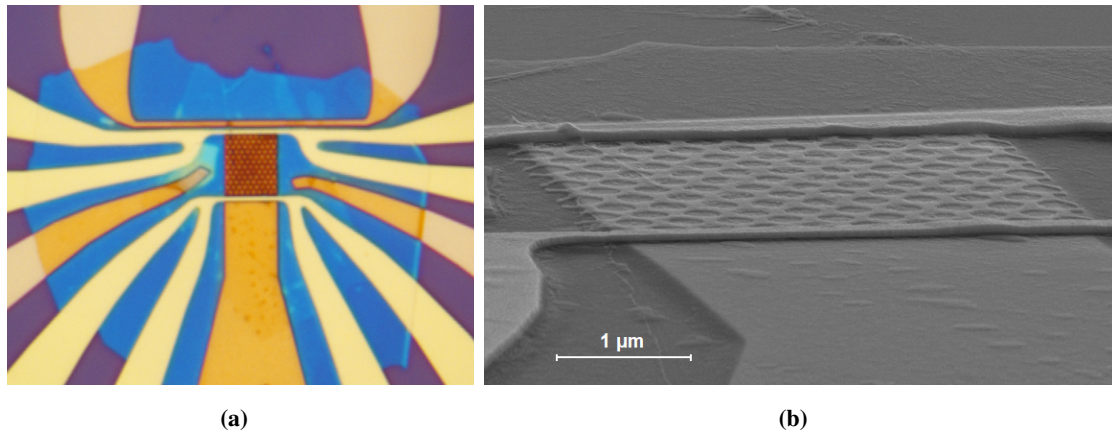


**Figure 11:** (a) Device after O<sub>2</sub> plasma. Graphene out of the Al mask has been etched completely. (b) Detail of the final device observed by SEM.

## 4.2 AFM analysis

The fabricated samples are analyzed by Atomic Force Microscopy (AFM)<sup>[45]</sup>. AFM is one of the most common types of Scanning Probe Microscopy techniques allowing high resolution imaging at the atomic scale by means of a probe interacting with a surface by different physical mechanisms (tunneling, force,...). In AFM, the forces developed between the tip and the surface are measured by detecting the deflection of a cantilever holding the tip. A feedback loop allows to adjust continuously the tip-surface distance while scanning, resulting in a high resolution topographical image. A laser impinges on the top of the cantilever and it is deflected onto a photodetector, enabling the continuous monitoring of the tip position. For our devices, we use the so called tapping mode: the cantilever (PPP-NCHR) oscillates with a frequency close to its resonant one ( $\sim 330\text{kHz}$ ), and the feedback loop is set on the oscillation amplitude, which is maintained constant.

A representative AFM image of a representative fabricated sample (S45, nanomeshed) is shown in Fig.12a, and a zoom on the graphene nanomesh as well as on the border of the hBN flake is given in Fig.12b and Fig.12c, respectively. AFM analysis is used to characterize the thicknesses of the various flakes. By means of the Gwyddion software, we extract the profiles of the various layers in the devices and we measure their thicknesses, as shown in Fig.12d and Fig.12e, for a representative example of nanomeshed graphene and hBN, respectively. These profile lines are extracted following the blue and green lines of Fig.12b and Fig.12c. Note that the reported heights are the average over sets of ten measurements for each considered step. Moreover, in the particular case of Fig.12, the thickness of graphene holes is higher than the one of the original graphene flake due to an over etching of the hBN layer below. When possible we have performed

the thickness analysis before the nanomeshing procedure. Otherwise a rough thickness estimate can be obtained by measuring the step profiles in differently etched regions. The typical thicknesses of the graphene flake in samples fabricated during my internship are in the range of 2.5 nm - 8 nm, while that of hBN flakes are in the range of 20 nm - 50 nm.

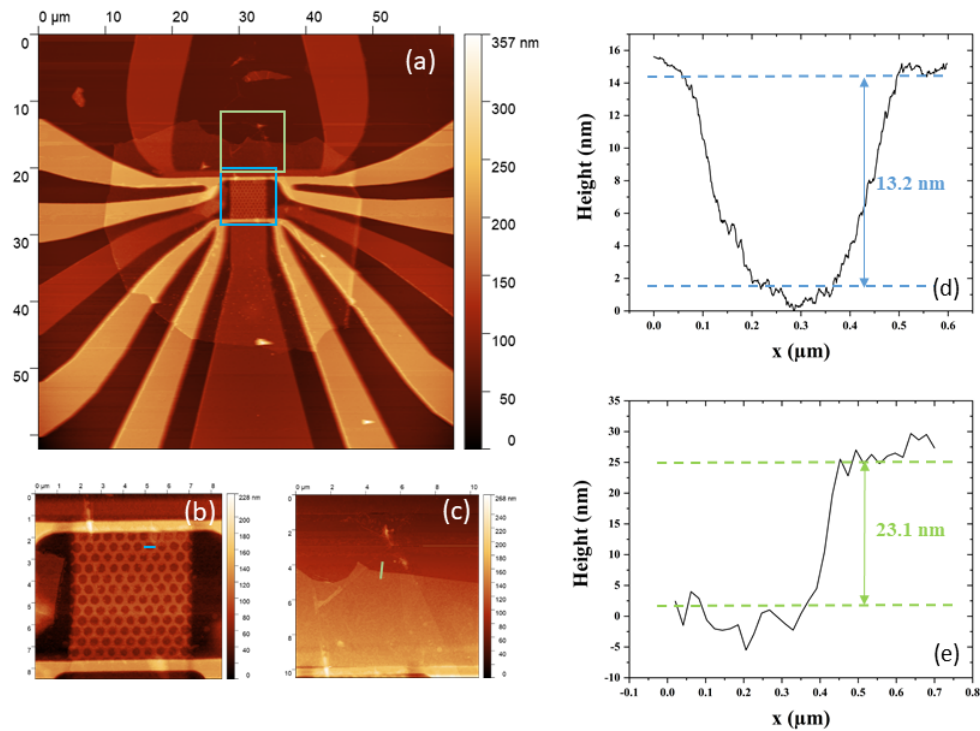


**Figure 12:** (a) AFM image of the whole sample of a graphene based nanomeshed device (S45). (b) Detail of graphene nanomesh in blue square of Fig.(a). (c) Detail of the hBN in green square of (a). (d) Height profile for graphene holes following the blue line in (b). (e) Height profile for hBN following the green line in (c).

## 5 Thermoelectric characterization protocol

The measurement set-up for electric and thermoelectric characterization is based on a 14-probes Nextron micro-probe station (Fig.13) that allows measurements under vacuum ( $P \sim 10^{-6}$  mbar) with temperature control (resolution  $0.1^\circ\text{C}$ ) from room to  $700^\circ\text{C}$ .

The high number of probes is required to contact the different electrodes of the device. Different circuitual schemes are involved, in order to achieve the electric and thermoelectric characterization of the devices.

Before the measurements, an annealing step<sup>[46]</sup> at  $400^\circ\text{C}$  is performed for 40 minutes in order to remove water and improve the cleaning of the device surface.



**Figure 13:** Nextron micro-probe station.

Moreover, 15 cycles of current annealing at  $200 \mu\text{A}$  are performed in the metallic electrodes/thermometers nanowires, allowing to stabilize their resistances. In the following section, the complete characterization protocol is explained, by reporting as an example experimental measurements obtained for a non-nanomeshed sample (S39).

## 5.1 Thermometers calibration

The first step required in the measurement protocol is the calibration of the thermometers. The sample temperature is increased by step of  $2^\circ\text{C}$  from  $30^\circ\text{C}$  to  $50^\circ\text{C}$  and for each steps a 4-points measurement of the resistance is done by injecting a small current ( $\sim 40\mu\text{A}$ ) in each of the thermometers with two Yokogawa 7651 sources and measuring the voltage drop on the nanowires with two Keithley 2182A nanovoltmeters, following the scheme of Fig.14a.

From the I-V characteristics, we extract the temperature dependence of the nanowire resistances, that are fitted following the linear model

$$R = R_o + \beta(T - T_o)$$

as shown in Fig.14b. This calibration allows to find the parameter  $\beta$  and  $R_o$ , that will be used in the next step, allowing to extract the thermometer temperature from the measurements of the resistance value.

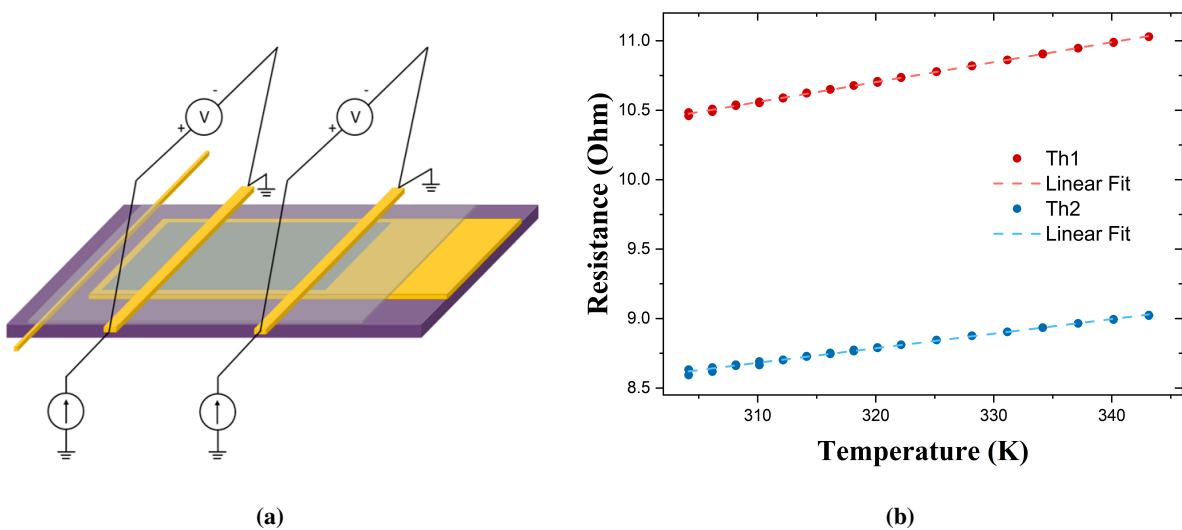


**Figure 14:** (a) Circuital scheme for thermometers calibration. (b) Calibration results.

## 5.2 Temperature gradient calibration

The second step of the measurement protocol is the calibration of the temperature gradient that can be achieved in the longitudinal direction of the device by Joule heating of the micro-heater. In this case, the external temperature is kept fixed ( $35^\circ\text{C}$ ), while a current  $I_H$  is injected into the heater by

means of a third current source. The temperature gradient  $\Delta T$  induced between the thermometers is measured by exploiting the results of the previous calibration. The scheme of the circuit used to achieve this step is shown in Fig.15a.

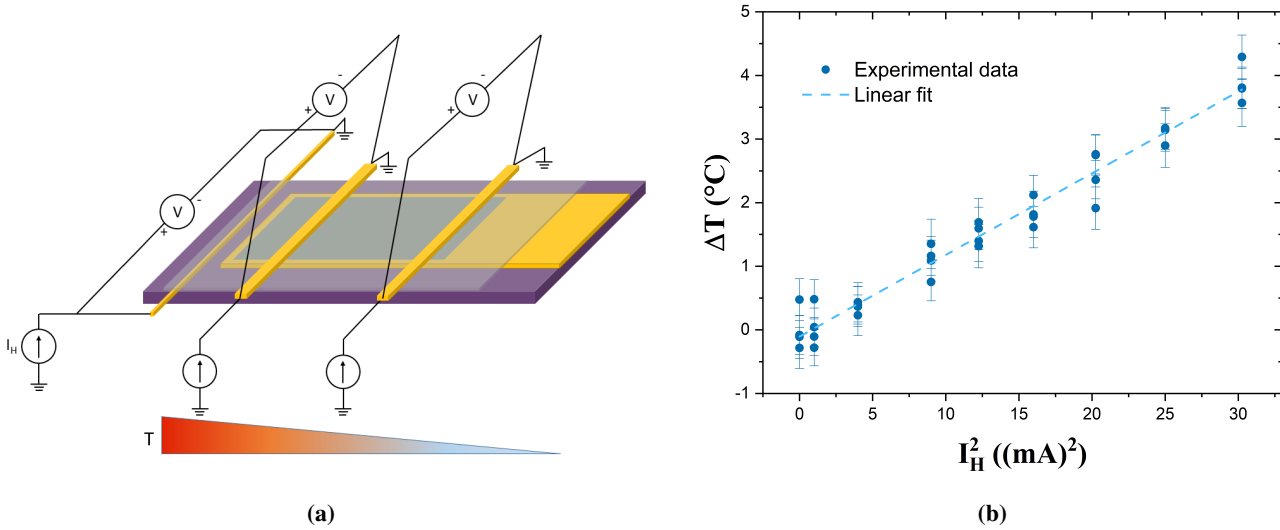


**Figure 15:** (a) Circuitual scheme for temperature gradient calibration. (b) Calibration results.

The aim of this second calibration is instead to extract the dependence of  $\Delta T = \Delta T(I_H)$ . The model used for the fitting is quadratic, due to the expected quadratic dependence of Joule heating effect on the current. We use a fitting of the type

$$\Delta T = aI_H^2 + bI_H + c$$

where the quadratic coefficient is directly related to the heating, while the constant term and the linear one take into account for instrumental offset and small leakage between the heater and the thermometers. A linear fitting  $\Delta T(I_H^2) = aI_H^2 + c$  is also provided in Fig.15b, showing that the quadratic term is dominating. Typical temperature gradients of the order of  $\sim 4\text{-}5^\circ\text{C}$  are achieved for a current in the heater of  $\sim 5\text{mA}$ .

### 5.3 Electrical and thermoelectric measurements

Electrical measurements allow to determine the device conductance and its dependence on the gate voltage. The scheme for the electrical characterization is depicted in Fig.16, where the first thermometer has the function of drain contact and is connected to the Yokogawa voltage source, while the second thermometer, acting as source contact, is connected at the input of a current-voltage amplifier Femto DLPCA-200, whose output is read by a Agilent 34401A multimeter. An example of I-V characteristic is shown in Fig.17a for a device including a graphene flake with a resistance of  $R \sim 0.13 \text{ k}\Omega$ .

The gate contact is connected to a second voltage source, so to control the charge carrier density in the graphene flake by applying a gate voltage. An example of transconductance measure-

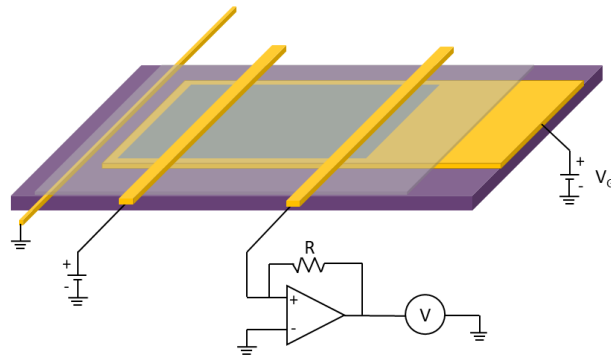


**Figure 16:** Circuitual scheme for the electrical characterization of the devices.

ment at  $V_{DS} = 10$  mV is shown in Fig.17b. In particular, it can be observed that a slight modulation of the conductance occurs over the explored voltage range, corresponding to a resistance modulation of  $\sim 5\%$ , the resistance varies in fact from  $R_{min} \sim 0.131$  k $\Omega$  to  $R_{max} \sim 0.137$  k $\Omega$ . Playing with graphene multilayer, this is not surprising, as a metallic-like behaviour is in principle expected. Moreover, note that for high values of  $V_G$ , the transcharacteristic is approaching plauetaus that could be indicative of the opening of leakage through the gate. For this reason, the range of gate voltages for which the following measurements are led is restricted in the interval given by these boundary values.

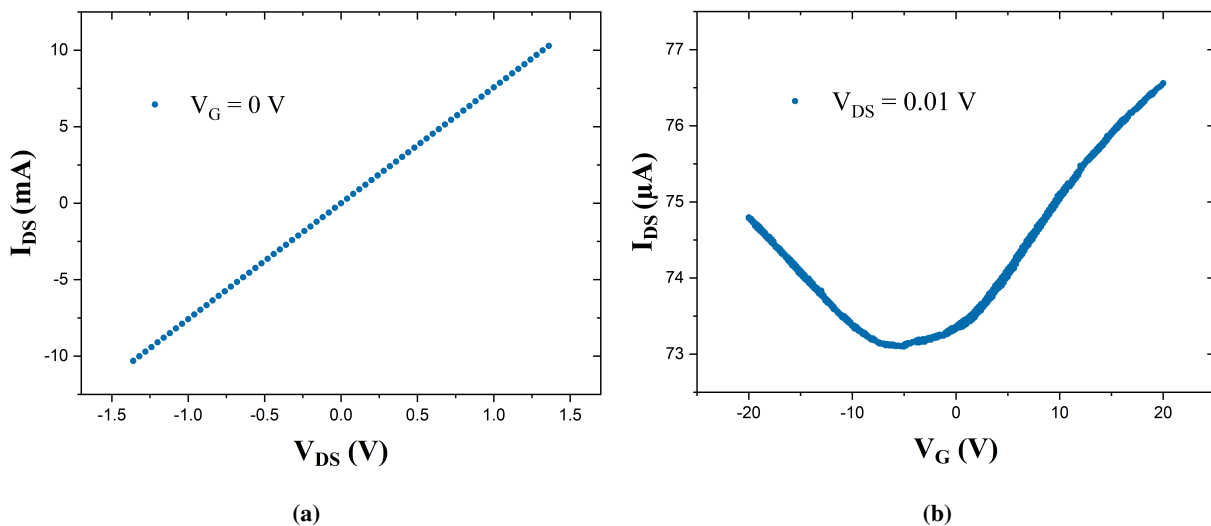


**Figure 17:** (a) I-V characteristic and (b) transcharacteristic of the GN based device.

#### 5.4 Seebeck coefficient measurement

To measure the Seebeck coefficient, the open-circuit voltage,  $V_{oc}$ , between the two thermometers is measured by a nanovoltmeter as a function of the current injected into the heater. The used

circuitual scheme is depicted in Fig.18.

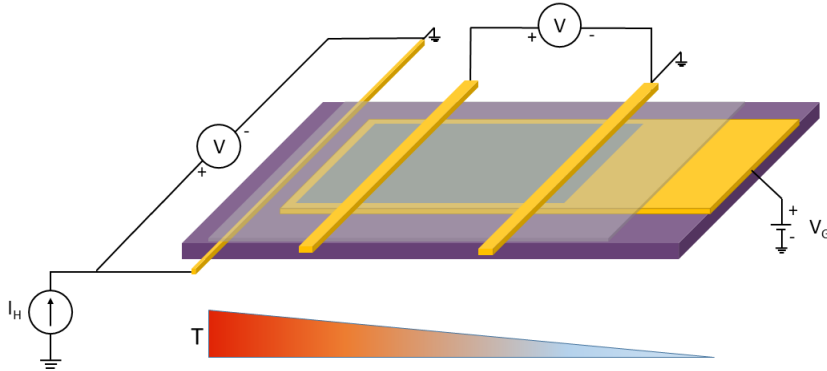


**Figure 18:** Circuitual scheme for Seebeck measurement.

To extract the thermoelectric voltage, a second order fitting of the kind

$$V_{oc} = a_0 + a_1 I_H + a_2 I_H^2$$

is considered. The three terms have different physical meanings<sup>[47]</sup>: the constant term  $a_0$  takes into account the nanovoltmeter offset, the linear term takes into account for possible leakage contributions between the heater and the gate and between the heater and the thermometers, and finally the second order term is the pure thermoelectric voltage,  $V_{th} = a I_H^2$ . Two examples of open-circuit voltage measurements as a function of the heating current are shown in Fig.19 for two different gate voltages. We can clearly see that the quadratic trend is the dominating one.

Note that for the different sign of the gate voltage the nature of the majority charge carriers generating the thermoelectric voltage is inverted, so for negative  $V_G$ , the fitting parabola will be concave and for positive  $V_G$  it will be convex.

The Seebeck coefficient is calculated considering the ratio between the extracted thermoelectric voltage and the temperature gradient correspondent to the heater current as measured by the calibration step of §5.2:

$$S = -\frac{V_{th}}{\Delta T} = -\frac{a_2}{a}.$$

This whole procedure is repeated iteratively for many gate voltages at the fixed temperature of 35°C in order to find its dependence for the Seebeck coefficient, as shown in Fig.20. In the figure we see that  $|S|$  reaches a maximum value of 20  $\mu\text{V}/\text{K}$ . Moreover we can note that the inversion in the Seebeck coefficient sign occurs around  $V_G = -10\text{V}$ , indicating that at zero gate voltage the flakes show dominating charge carrier density due to electrons.

## 5.5 Thermoreflectance Measurements

During my internship, I have been partially involved in a first attempt of measuring the thermal conductivity of nanomeshed graphene by means of the modulated thermoreflectance (MTR) tech-

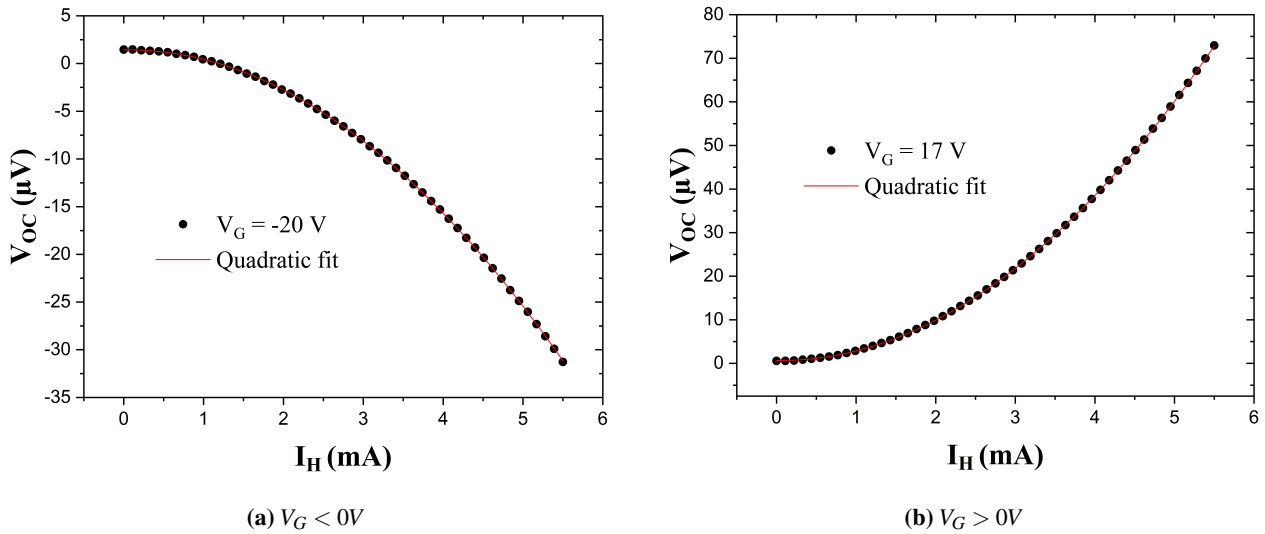


**Figure 19:** Thermal voltage obtained for different values of current passing through the heater.

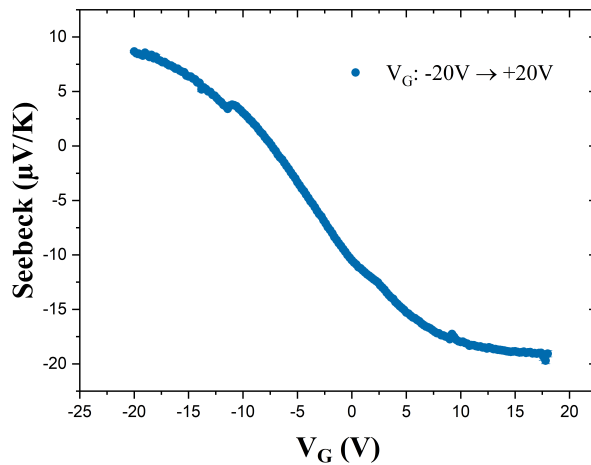


**Figure 20:** Seebeck coefficient as a function of the gate voltage for the GN based device (S39).

nique, in the framework of a collaboration at the Institut Des Nanosciences De Paris (INSP), at Sorbonne Université.

The working principle<sup>[48]</sup> of the thermoreflectance measurement is based on a pump-probe approach with two lasers with different wavelengths (Fig.21). A green beam (pump) is used to heat locally the sample, inducing a gradient of temperature. The reflectivity of the material is measured by a blue laser (probe) depending upon the local temperature of the scanned point. Being the pump modulated ( $10 \text{ kHz} \leq f \leq 1 \text{ MHz}$ ), we measure the reflectance modulated by the temperature. By scanning on all the surface by the probe laser or (as in our case) by the pump laser, information can be obtained about the heat propagation inside the sample. The thermal diffusion length  $\mu$ , which is the characteristic length associated to the propagation of the heat wave into the material, it is

linked to the diffusivity  $D$  and the modulation frequency  $f$  by the relation  $\mu = \sqrt{D/(\pi f)}$ , where the diffusivity is defined by  $D = \kappa/(\rho C)$ , where  $\kappa$  is the thermal conductivity,  $\rho$  is the mass density and  $C$  is the specific heat.

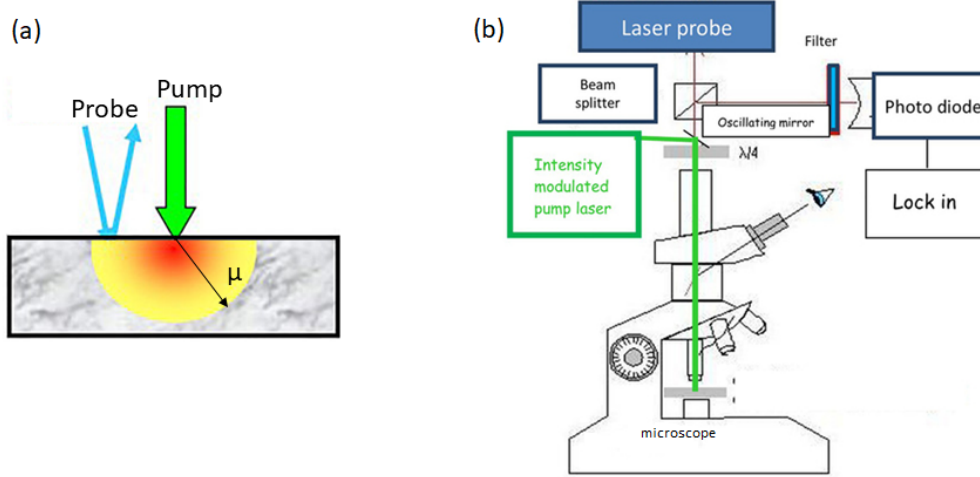


**Figure 21:** (a) Scheme for pump-probe approach in MTR. (b) Experimental set-up used for the thermoreflectance measurement. Extracted from [48].

By solving the Fourier law

$$\kappa \left( \frac{\partial^2 T(r, z, t)}{\partial z^2} + \frac{\partial^2 T(r, z, t)}{\partial r^2} + \frac{1}{z} \frac{\partial T(r, z, t)}{\partial r} \right) = \rho C \frac{\partial T(r, z, t)}{\partial t}. \quad (3)$$

the theoretical expression for the temperature profile is given by

$$T(r, 0, t) = \frac{Q}{2\pi\kappa r} \exp\left(-\frac{r}{\mu}\right) \exp\left(i\left(\omega t - \frac{r}{\mu}\right)\right) \quad (4)$$

where  $Q$  is the heat injected into the system.

The signal coming from this experiment is proportional to the optical reflection variation  $\partial R_{probe}/\partial T$  induced by the temperature. We measure the amplitude and the phase of the signal which is fitted on a theoretical model based on equation 4, where the fit parameters are  $\kappa_{//}$  and  $\kappa_{\perp}$ .

Although this technique has its major applications for the analysis of bulk samples, the thermal conductivity of thin films down to  $\sim 20$  nm have been evaluated with it<sup>[48]</sup>. However, this is the first attempt to use MTR to extract the thermal conductivity of a 2D material based device. The main difficulty encountered is related to the reduced material thickness with respect to the thermal diffusion length (which is found to be  $\sim 300$  nm by using the values of ref.[25] for a frequency of 1 MHz). This implies that the entire structure has to be taken into account in analyzing heat diffusion. Moreover, heat dissipation in the perpendicular direction between the different 2D materials dominates and interface thermal resistances are scarcely distinguished.

As a consequence, we measure the sample layer by layer (we extract  $\kappa$  of gold with a measurement in a region in which only the gold is present, then we extract  $\kappa$  for hBN with measurements

done in a region in which only Au and hBN are present, by fixing Au properties by the precedent analysis, and finally the measurement over the stake GN/hBN/Au can be used to extract GN properties, having measured hBN/Au properties before). In this way the possible influence of the signal of the layers underneath is always taken into account.

## 6 Results and discussion

During my internship, I have fabricated 60 devices, and successfully completely characterized 11 of them. In the following section, a comparison between two representative devices (S39, non-nanomeshed, and S44, nanomeshed) with similar 2D flakes thicknesses is done, in order to quantify the modifications of the properties due to the nanostructuring of the graphene multilayer. All measurement have been done at 35°C. The main geometrical parameters of these two samples are given in Table 1.

	$d_{\text{hBN}}$	$d_{\text{GN}}$	$R$ (nominal)	$h$ (nominal)
S39	$23.7 \pm 1.2$ nm	$4.7 \pm 0.5$ nm	-	-
S44	$48.4 \pm 3.4$ nm	$4.4 \pm 1.4$ nm	200 nm	150 nm

**Table 1:** Values for thickness of hBN ( $d_{\text{hBN}}$ ), graphene ( $d_{\text{GN}}$ ) for S39 and S44.  $R$  is the radius of the nanomesh holes,  $h$  is the previously defined neck width.

It has to be noticed that in showing results, the gate voltages have been normalized by the thickness of the hBN flake. In fact, the gate coupling depends on the capacitive effect of the FET-like structure, so for the same applied voltage, different hBN thicknesses correspond to different shifts in the Fermi level.

### 6.1 Electric and thermoelectric properties

An important parameter involving the characterization of the sample is the electrical conductivity of the nanomeshed channel, since it is a key figure to obtain the quantities determining the strength of the Thermoelectric Effect, such as the power factor.

The electrical conductivity could canonically be found by using the second Ohm's law

$$R = \frac{1}{\sigma} \frac{S}{L}, \quad (5)$$

where  $L$  is the length of the channel and  $S = W \times d$  is the section of the channel, with  $W$  width of the section and  $d$  the thickness found with the AFM analysis. However, equation 5 can be rigorously applied only in case of a regular slab of material. So in the case of a nanomeshed sample a correction has been applied to take into account the non-uniformity induced by the pores. Although further modeling could be needed to obtain a more rigorous expressions for the electrical conductivity of this kind of structures, as a rough estimation we can consider an effective section for the nanomeshed flake calculated as

$$S_{\text{NM}} = V_{\text{NM}}/L$$

where  $V_{NM} = V - V_{pores}$  is the volume of the real sample, calculated by subtracting the volume of the pores  $V_{pores} = n\pi r^2 t$  (with  $n$  number of pores and  $r$  radius of the pore) from the volume  $V$  of the non nanomeshed flake. Moreover, the resistance can be obtained by calculating the ratio between drain source voltage (set constant to 10 mV) and current for the different gate voltages. Following this approach, we can compare the conductivity of the nanomeshed (both with and without correction) and non nanomeshed sample, as it can be seen in Fig.22a for the two selected samples, S39 and S44.

We can note that, even if dealing with different samples, they show a very similar modulation trend of the electrical conductivity  $\sigma$  as a function of the applied gate voltage  $V_G$ , with a similar position of the minimum conductivity. This is not surprising since both have similar flakes thicknesses and they have been also fabricated almost simultaneously and with the exact procedure. As expected, nanomeshing induces a reduction of the value of  $\sigma$ , which is reduced by a factor of  $\sim 2$ . Most probably, the origin of such a reduction has to be found in the increased charge carrier scattering due to the presence of the pores and the residues of the nanofabrication patterning.

We can analogously compare the Seebeck measurement as a function of the gate voltage for the two samples. The two Seebeck coefficients are plotted in Fig.22b.

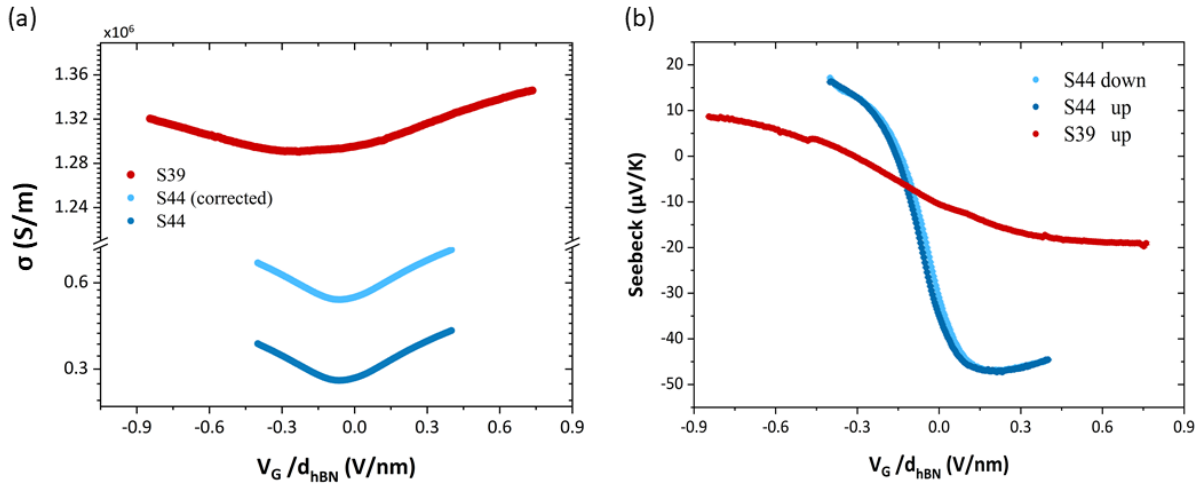


**Figure 22:** Comparison of (a) electrical conductivity and (b) Seebeck coefficient between nanomeshed and non-nanomeshed sample.

The Seebeck coefficient shows an enhanced behaviour for the samples with nanomesh. In both cases, at zero gate voltage the sample have an electron dominated density of charge carriers. Remarkably, the Seebeck coefficient increases in the case of the nanomeshed sample, its maximum value is more than 2 times higher than the value measured in the non-nanomeshed case. The origin of such a increase could be traced back to a modification of the density of states (DOS) of the material or to energy filtering effect once the nanomeshing is introduced.

## 6.2 Power Factor

As presented in the introduction, the power factor (PF) is defined as

$$PF = S^2 \sigma.$$

On the basis of the previous measurements and analysis, we can calculate the PF for the two presented samples as a function of the gate voltage. The two PF are compared in Fig.23. As expected, we see clearly that the PF is enhanced by a factor of  $\sim 2$  when nanomeshing multilayer graphene. This is an encouraging results, by considering that these are the first attempts in characterizing the thermoelectric properties of graphene nanomeshes. In real devices, by reducing the graphene thickness and optimizing the nanomesh structure, we should be able to further improve the measured PF. Furthermore, it can be noticed that the obtained values are comparable to what is commonly measured in literature for 2D materials<sup>[47]</sup>.

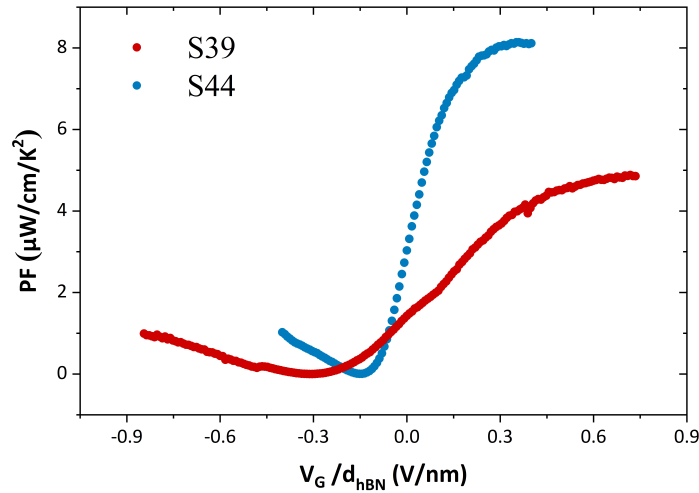


**Figure 23:** Power factor as a function of the applied gate voltage.

## 6.3 Thermoreflectance results

In the following, the results obtained with modulated thermoreflectance technique for two samples, nanomeshed (S46) and non-nanomeshed (S56), will be shown. Table 2 reports the thicknesses extracted by the AFM analysis for the two samples.

	$d_{Au}$	$d_{hBN}$	$d_{GN}$
S56	$50 \pm 1$ nm	$32 \pm 4$ nm	$6.4 \pm 0.9$ nm
S46	$45 \pm 1$ nm	$39 \pm 4$ nm	$2.7 \pm 1.5$ nm

**Table 2:** Values for thickness of gold ( $d_{Au}$ ), hBN ( $d_{hBN}$ ), graphene ( $d_{GN}$ ) for S56 and S46.

In Fig.24, the experimental data and correspondent best fitting curves are shown for the measurement of the MTR signal (amplitude and phase) for the graphene based device (a-b) and the GNM based device (c-d) at different frequencies.

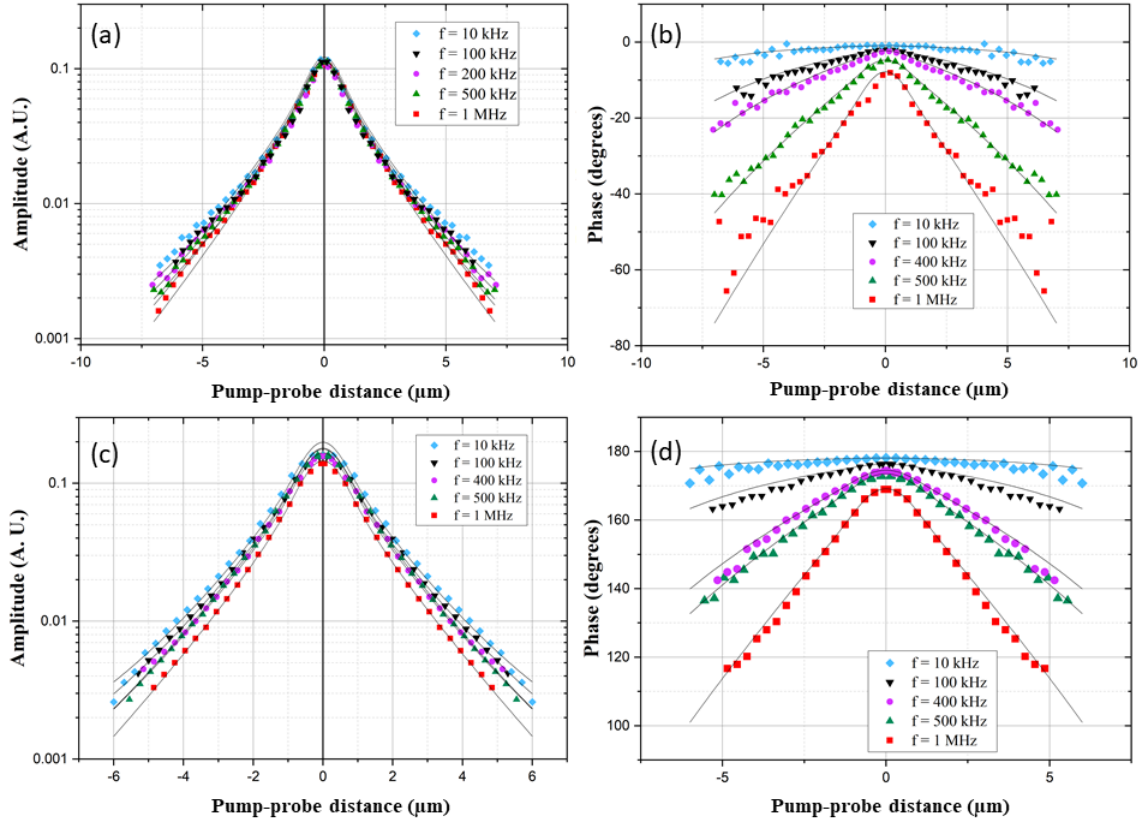


**Figure 24:** (a), (b) Amplitude and phase for MTR measurement for graphene of sample S56 (non nanomeshed). (c), (d) Amplitude and phase for MTR measurement for graphene of sample S46 (nanomeshed). The black lines are the fitting curves.

The final results obtained for the various layers are shown in Table 3. It has to be noticed that the reported ranges of values correspond to the interval well fitting the data. For the graphs in Fig.24  $\kappa_{//}$  and  $\kappa_{\perp}$  values in the middle of the ranges have been used.

	$\kappa_{Au}$	$\kappa_{hBN//}$	$\kappa_{hBN\perp}$	$\kappa_{GN//}$	$\kappa_{GN\perp}$
S56	$82 \pm 15$ W/(m·K)	170-270 W/(m·K)	2 W/(m·K)	400-800 W/(m·K)	6 W/(m·K)
S46	$95 \pm 15$ W/(m·K)	80-180 W/(m·K)	2 W/(m·K)	100-500 W/(m·K)	6 W/(m·K)

**Table 3:** Thermal conductivity values for the various layers of the samples S56 and S46.

Some critical aspects can be identified. First of all, thin gold layers are expected to have a thermal conductivity which is  $\sim 65\%$  of the bulk value<sup>[49]</sup>, while the result found here reports something on the order of  $\sim 23\%$ . The cause for this phenomenon, according to the previous experiences of the team, can be identified in the temperature annealing procedure that is done

prior to measurements, that evidently strongly modifies gold properties.

Furthermore, the perpendicular thermal conductivities can be varied over a wide range (1-10 W/(m·K) for hBN and 1-20 W/(m·K) for GN) without affecting notably the fitting. As a consequence, their values are fixed according to the literature<sup>[50],[25]</sup>.

Finally, although the range for the parallel thermal conductivity doesn't allow to determine with precision its value, it is clear that passing from a non-nanomeshed sample (S56) to a nanomeshed one (S46) implies a lowering of its value, confirming that nanostructuring worsen phonon transport.

By means of these values for the thermal conductivity and of the previously found values for the power factor, it is possible to obtain a first estimate of the figure of merit  $ZT$ , which results to be  $\sim 8 \times 10^{-4}$  and  $\sim 2.5 \times 10^{-4}$  at room temperature for the nanomeshed and non-nanomeshed graphene, respectively. Although these values are low, nanostructuring has ultimately induced an improvement of a factor higher than 3.

## 7 Conclusions and future perspectives

During my internship, I have fabricated devices which could allow the study of the thermoelectric properties of graphene nanomesh structures. The devices are made up of a periodically patterned multilayer graphene flake, used as central element in a FET-like configuration, with a bottom gate metallic electrode separated by a hexagonal boron nitride flake, acting as a dielectric spacer. I was particularly involved in the optimization of nanomeshing processing; the use of a thin metallic Al-mask turns out to be the best solution to obtain uniform and well-defined holes in graphene with typical diameter of 400 nm. The thicknesses of the different 2D materials building the device have been measured by AFM. Moreover, the graphene nanomesh has been electrically and thermoelectrically characterized by means of two gold nanowires that served as local thermometers and a thinner one that served as local heater.

Although a complete characterization has been done for more samples, I have presented in the report results on two representative couples of devices with and without nanomesh, which have similar 2D flakes thicknesses and have been fabricated simultaneously. By comparing the electrical conductivity and the Seebeck coefficients measurements on the two samples, I have shown that the first is reduced by a factor of  $\sim 2$  while the second is increased by a factor of  $\sim 2$ , resulting in an improved PF.

Furthermore, a first estimate of the thermal conductivity has been obtained by applying the MTR technique, showing a reduction with respect to the non nanomeshed case, as expected.

These results allowed us to estimate an improved figure of merit  $ZT$ , asserting the potential interest of nanostructuring 2D materials for engineering thermoelectric devices. Reducing the graphene flake thickness and optimizing the nanomesh geometry are surely the future direction of this work. Furthermore at long term, playing with the shape of the pores could represent a way to control the anisotropy of the different parameter defining the energy conversion efficiency.

## References

- [1] IEA (International Energy Agency). “Electricity Market Report”. In: (2022).
- [2] Jin-Cheng Zheng. “Recent advances on thermoelectric materials”. In: *Front. Phys. China* 3(3): 269-279 (2008).
- [3] Eric Pop. “Energy Dissipation and Transport in Nanoscale Devices”. In: *Nano Res* 3 147-169 (2010).
- [4] F. D. Rosi. “THERMOELECTRICITY AND THERMOELECTRIC POWER GENERATION”. In: *Solid State Electronics* 11 833-868 (1967).
- [5] Xu Dongchao. “Thermoelectric Studies of Nanoporous Thin Films and 2D materials”. In: *The University of Arizona* (2019).
- [6] Stephen Blundell. *Concepts in thermal physics*. Oxford University Press, 2010.
- [7] M. Huijben P. Brinks. “Thermoelectric oxides-Epitaxial growth of metal oxides”. In: *Woodhead Publishing Series in Electronic and Optical Materials* 397-441 (2015).
- [8] Y. M. Zuev et al. “Thermoelectric and magnetothermoelectric transport measurement of graphene”. In: *Phys. Rev. Lett.* 102 0968075 (2009).
- [9] B Sherman et al. “Calculation of Efficiency of thermoelectric devices”. In: *Journal of Applied Physics* 31 1 (1960).
- [10] Jack P. Holman. *Thermodynamics*. New York: McGraw-Hill, 1980.
- [11] P. Dollfus et al. “Thermoelectric effects in graphene nanostructures”. In: *J Phys Condens Matter* 27 13 (2015).
- [12] A. Dehkordi et al. “Thermoelectric power factor: Enhancement mechanisms and strategies for higher performance thermoelectric materials”. In: *Materials Science and Engineering R* 97 1-22 (2015).
- [13] N. H. March J. Williams. *Theoretical Solid State Physics*. 1985.
- [14] T. G. Novak et al. “2D and 3D nanostructuring strategies for thermoelectric materials”. In: *Nanoscale* 11 19684 (2019).
- [15] S. Lee et al. “Ferroelectric-thermoelectricity and Mott transition of ferroelectric oxides with high electronic conductivity”. In: *Journal of the European Ceramic Society* 32 16 3971-3988 (2012).
- [16] M. S. Dresselhaus et al. “New Directions for Low-Dimensional Thermoelectric Materials”. In: *Advanced Materials* 19, 1043 (2007).
- [17] G. J. Snyder and E. S. Toberer. “Complex thermoelectric materials”. In: *Nature Materials* 7, 105 (2008).
- [18] M. S. Dresselhaus et al. “Low-dimensional thermoelectric materials”. In: *Physics of the Solid State* 41, 679 (1999).

- [19] A. Fabiam-Mijangos and J. Alvarez-Quintana. *Thermoelectric Devices: Influence of the Legs Geometry and Parasitic Contact Resistances on ZT*. 2018.
- [20] P. Dolphus et al. “Thermoelectric effects in graphene nanostructures”. In: *Journal of Physics: Condensed Matter* 27 133204 (2015).
- [21] Mikhail I. Katsnelson. “Graphene: carbon in two dimensions”. In: *Materials today* 10 1-2 (2007).
- [22] K. S. Novoselov et al. “Electric Field Effect in Atomically Thin Carbon Films”. In: *Science* 306 5696 (2004).
- [23] A. C. Neto et al. “Drawing conclusions from graphene”. In: *Phys. World* 19 (11) 33 (2006).
- [24] D. R. Cooper et al. “Experimental Review of Graphene”. In: *ISRN Condensated Matter Physics* 2012 501686 (2011).
- [25] E. Pop et al. “Thermal properties of graphene: Fundamentals and applications”. In: *Materials Research Society* 37 (2012).
- [26] Y. Xu et al. “Thermal and Thermoelectric Properties of Graphene”. In: *Small* 10 11 (2014).
- [27] D. S. Schulman et al. “Contact Engineering for 2D materials and devices”. In: *Chem. Soc. Rev.* 47 3037 (2018).
- [28] M. M. Sadeghi et al. “Phonon-interface scattering in multilayer graphene on an amorphous support”. In: *Proceedings of the National Academy of Sciences* 110 16321 (2013).
- [29] S. Timpa et al. “Role of metal contacts on the electric and thermoelectric response of hBN/WSe<sub>2</sub> based transistors”. In: *Journal of Applied Physics* 130 185102 (2021).
- [30] D. Maroudas L. Hu. “Thermal transport properties of graphene nanomeshes”. In: *Journal of Applied Physics* 116 184304 (2014).
- [31] J. Bai et al. “Graphene nanomesh”. In: *Nature Nanotechnology* 5 (2010).
- [32] W. Oswald and Z. Wu. “Energy gaps in graphene nanomeshes”. In: *Physical Review B* 85 115431 (2012).
- [33] L. Yang et al. “High Performance Thermoelectric Materials: Progress and Their Applications”. In: *Advanced Energy Materials* 8 1701797 (2018).
- [34] A. J. Minnich et al. “Bulk nanostructured thermoelectric materials: current research and future prospects”. In: *Energy Environ. Sci.* 2 466-479 (2009).
- [35] W. Tse et al. “Ballistic hot electron transport in graphene”. In: *Applied Physics Letters* 93 023128 (2008).
- [36] J. Duan et al. “High thermoelectric power factor in graphene/hBN devices”. In: *PNAS* 113 50 (2016).
- [37] K. Zhang et al. “Two dimensional hexagonal boron nitride (2D-hBN): synthesis, properties and applications”. In: *Journal of Materials Chemistry C* 5 11992 (2017).

- [38] J.-U. Lee et al. “Thermal conductivity of suspended pristine graphene measured by Raman spectroscopy”. In: *Phys. Rev. B* 83 081419 (2011).
- [39] S. Chen et al. “Raman measurements of thermal transport in suspended monolayer graphene of variable sizes in vacuum and gaseous environment”. In: *ACS Nano* 5 321 (2011).
- [40] A. A. Baladin. “Thermal properties of graphene and nanostructured carbon materials”. In: *Nat. Mater* 10 569 (2011).
- [41] J. H. Seol et al. “Two-dimensional phonon transport in supported graphene”. In: *Science* 328 213 (2010).
- [42] J. H. Seol et al. “Thermal Conductivity Measurement of Graphene Exfoliated on Silicon Dioxide”. In: *Journal of Heat Transfer* 133 022403 (2010).
- [43] W. Jang et al. “Thermal conductivity of suspended few-layer graphene by a modified T-bridge method”. In: *Appl. Phys. Lett.* 103 133102 (2013).
- [44] X. Wang and H. Dai. “Etching and narrowing of graphene from the edges”. In: *Nature Chemistry* 2 (2010).
- [45] G. Binnig et al. “Atomic Force Microscope”. In: *Phys. Rev. Lett.* 56 930 (1986).
- [46] S. Timpa. *Electric and thermoelectric properties of supported 2D materials*. Université de Paris, 2021.
- [47] M. Kayyalha et al. “Gate-tunable and thickness-dependent electronic and thermoelectric transport in few-layer MoS<sub>2</sub>”. In: *Journal of Applied Physics* 120 134305 (2016).
- [48] D. Fournier et al. “Measurement of thermal properties of bulk materials and thin films by modulated thermoreflectance (MTR)”. In: *Journ. Appl. Phys.* 128 241101 (2020).
- [49] K. Nishimura et al. “Measurement of in-plane thermal and electrical conductivities of thin film using a micro-beam sensor: A feasibility study using gold film”. In: *International Journal of Heat and Mass Transfer* 95 727-734 (2016).
- [50] Y. Gong et al. “Two-Dimensional Hexagonal Boron Nitride for Building Next-Generation Energy-Efficient Devices”. In: *ACS Energy Letters* 6(3) 985-996 (2021).